



High current speed events in a harbor channel driven by resonant sub-hourly sea level dynamics: an example from Varna, Black Sea

Jüri Elken¹, Laura Piho², Maarja Kruusmaa²

¹Department of Marine Systems, Tallinn University of Technology, Tallinn, EE12618, Estonia

5 ²Centre for Biorobotics, Tallinn University of Technology, Tallinn, EE12618, Estonia

Correspondence to: Jüri Elken (juri.elken@taltech.ee)

Abstract. Current and sea-level observations in the 2.4-km-long, 300-m-wide channel between Varna Lake and the Black Sea, conducted by three novel Hydromast stations with a 1-minute resolution, revealed that moderate sub-hourly dynamics were occasionally interrupted by high-amplitude oscillations with a period of a few tens of minutes. The resonant excitation of the events was studied using barotropic 1D analytical and numerical models. Basic features of high-intensity sub-hourly variations can be interpreted as linear barotropic long waves in a sea-channel-lake system with resonant and damped forcing. The observed 37-minute oscillations, identified from the power spectra, spectrogram, and wavelet analysis, can be explained as the first mode of the channel-lake system. Another period of 19 minutes resembles the zero, quarter-wave mode of the channel and the second mode of the channel-lake system. During the measurement period, two high-amplitude events were highlighted. One of the events is interpreted as having been caused by a meteotsunami; moderate meteorological conditions prevailed; strong channel oscillations began abruptly and lasted for a few cycles. The second event occurred more than 5 h after landward winds up to 20 m s^{-1} . The observed maximum changes in current and sea level - up to 0.8 m s^{-1} and 0.8 m , respectively, over 10 minutes - are harmful to ship navigation, harbor operations, and coastal management. Building on these observations, approaches for detecting and forecasting strong sub-hourly oscillations are discussed.

20 **1 Introduction**

Coastal embayments and channels respond to forcing from the open sea, under the control of weather variability, in a multitude of physical mechanisms. It was discovered a long time ago that coastal dynamics, encompassing waves, currents, and turbulence, may include tidal effects, barotropic and baroclinic self-oscillations (seiche) excited in topographically bounded domains, and different transformations of wind waves. An important component of variability arises from waves, which can be divided into short, non-hydrostatic waves with periods typically less than a minute, and long waves that are vertically in a hydrostatic balance and may be influenced by the Earth's rotation (LeBlond and Mysak, 1981).

Oscillations in semi-enclosed basins and channels (Miles, 1974; Rabinovich, 2009) include Helmholtz-type oscillations of a basin connected to the sea by a narrow channel (Miles and Munk, 1961; Méhauté et al., 1962), and seiche in elongated semi-enclosed basins (Giese and Chapman, 1993; see also the textbook by Cushman-Roisin and Beckers, 2011). The seiches



30 often have half-wave (Cummins et al., 2010) or quarter-wave (Cerralbo et al., 2014; Zheng et al., 2024) character. Both wave
types may exhibit resonant responses to external forcing (Miles and Lee, 1975) and include nonlinear effects (Maas, 1997;
Doelman et al., 2002). The resonant modes are often associated with the diurnal or semidiurnal tides (Maas, 1997; Luettich
et al., 2002). Sub-hourly oscillations with a period of a few tens of minutes may be excited during atmospheric low-pressure
35 events when stronger high-frequency atmospheric pressure disturbances occur (Sammartino et al., 2014). At sub-hourly
periods, moving atmospheric pressure systems can generate coastal edge waves on the ocean side of channels and river
mouths (Sun and Niu, 2021) and form meteotsunamis through Proudman resonance, when the transient speed of weather
patterns equals the phase speed of long gravity waves (Williams et al., 2021; Vilibić et al., 2025).

Ocean state observations and forecasts are usually exchanged at 1-hour intervals, which is sufficient for detecting the
main features of tides and storm surges. However, the need for sub-hourly resolution in routine meteorological and
40 oceanographic data was recognized as early as the 1950s (Van der Hoven, 1957), who showed spectral peaks in wind data at
about 1 minute. In coastal oceanography, water levels are recorded at 1-minute intervals in many locations since the 1980s
(Miller and Luscher, 2019). Presently, there are initiatives to manage high-resolution water level data, such as SHELDA
(Sub-hourly European Quality Controlled Sea Level Dataset; Balić and Šepić, 2025), but standard data exchange for now
and forecasts, such as in Copernicus Marine Service, uses a 1-hour resolution.

45 Sub-hourly water dynamics contribute to the (1) extremely high water levels during the storm surges (Medvedev et al.,
2022; Ruić et al., 2023), (2) anatomy of seismic tsunamis (Catalán et al., 2025), (3) events of high currents at topographic
constrictions (even when water level disturbances are small), disturbing navigation and/or impacting the sediments and
coastline (Seo et al., 2024; Kanarik et al., 2025).

Detection and analysis of sub-hourly dynamics are enabled by recent developments in observation techniques that make
50 high-frequency current observations available at moderate costs. Among the applications of these new methods, we note the
first presentation of the Varna Port Case Study (Egerer et al., 2025), which used Hydromast observations to study the
hydrodynamic patterns in the area. **The program was motivated and supported by the ILIAD project (<https://iliad-project.eu/>)
and contributed to the Digital Twins of the Ocean. One of the aims of the project is to determine the characteristics and
forcing mechanisms of hydrodynamical patterns that cause navigational problems.**

55 The present study aims to explore the events with high current speed associated with resonant sub-hourly sea-level
dynamics in the harbor system comprising a sea bay and narrow channels connecting to the upstream lake and river. The
study uses the same ILIAD data from the Varna Harbor area.

The paper is organized as follows. After the introduction, Chapter 2 presents the data and methods, beginning with a
description of the study area. The presentation of observations includes dedicated current and sea-level observations using
60 the Hydromast system, as well as background **sea-level** and meteorological observations conducted by the Bulgarian
research authorities. Data used from the EU Copernicus Marine Service are also outlined. Further subchapters present the
data analysis. Chapter 3 on results presents the observed water-level and current time series, together with meteorological
data, and analyzes sub-hourly variability. A detailed analysis of high-current-speed events follows oscillatory analysis. The



65 observed variability is subject to interpretation using a 1D shallow-water model outlined in the Appendix. In Chapter 4, the results are discussed with respect to the mechanisms driving high-current-speed events and the prospects for predicting them in the interests of port authorities and ship captains. Conclusions are presented in Chapter 5.

2 Data and Methods

2.1 Study area

70 The focus of the study is the marine area of the city of Varna, Bulgaria, located in the western part of the Black Sea (Fig. 1). The Black Sea is a deep (maximum depth about 2200 m) semi-enclosed sea in which freshwater input, together with restricted water exchange with the Mediterranean, forms an estuarine basin. The water masses have distinct vertical stratification; together with river input in coastal areas, density gradients and wind stress create cyclonic circulation of the sea, consisting of coastal rim current and unsteady circulation cells within the deep basins. Tides are rather weak in the Black Sea, with diurnal and semidiurnal periods having amplitudes typically less than 0.2 m in the sea level time series. There are 75 spectral signatures of large-scale self-oscillations (seiche) at periods 10.7, 5.8, 4.9, and 4.1 h (Medvedev, 2022).

On the seaside, the region of interest includes Varna Bay, the second-largest Bulgarian bay, with an approximate width of 3 km and a length of 5 km, defined by coastal capes. The currents and sea level of the western coastal region of the Black Sea are impacted by the hydrodynamics of the whole sea area (Stanev, 2005). West of Varna Bay lies Varna Lake, an 11- 80 km-long, 2-km-wide lake that receives freshwater from upstream Boleslaw Lake and the rivers. The lake is connected to the sea by two navigation channels. The Varna Lake-Varna Bay system facilitates freshwater inflow into Black Sea and saline seawater flow into Varna Lake (Yakushev et al., 2026). The depths of the region are shallow, up to 20 m in the Varna Bay and Varna Lake, and less in the navigation channels.

The study site is in a humid subtropical climate zone. The mean wind is oriented alongshore in the coastal sea area to the south (Stanev and Ricker, 2019). Regarding wind variability (mainly due to the passage of synoptic weather systems), 85 the wind rose (Panaitescu et al., 2023) shows mainly alongshore winds in either southerly or northerly directions. The winds are modified in the land-bound Varna Bay-Varna Lake system, located in a valley between the northern and southern hills. Orographic steering, combined with sea breezes, guides the winds cross-shore along the valley (Barantiev et al., 2011; Trukhchev et al., 2025). Storms are usually observed during winter, when cold air masses come from the north. Sea breezes occur during the warmer seasons; they may create strong diurnal signals in cross-shore winds and air temperature.

90 The area of interest has been largely influenced by intensive human activity for coastal protection and urban socio-economic development. The northern channel (Channel 3) is older, shorter, and narrower. It serves multiple terminals and plays a crucial role in managing large-ship traffic. The southern channel (Channel 1) is newer, longer, and wider, and is the main waterway connection between the Black Sea's Varna Bay and Lake Varna. The channels have a bending shape: they are rotated clockwise by about 20° from the west-east direction along the seaside and by about 40° near the lake.



95 The study was conducted in Channel 3, a 2.4-km-long channel located in the marine area of the city of Varna, within the Varna Port facilities. The aim was to gain a better understanding of flow directions and speeds in channels to aid pilots in navigating ships. The study was planned to advance knowledge of water movement patterns, which could support port management and navigation safety and contribute to environmental impact assessments. A long-term aim is to predict strong flows and promptly inform pilots about changing currents.

100

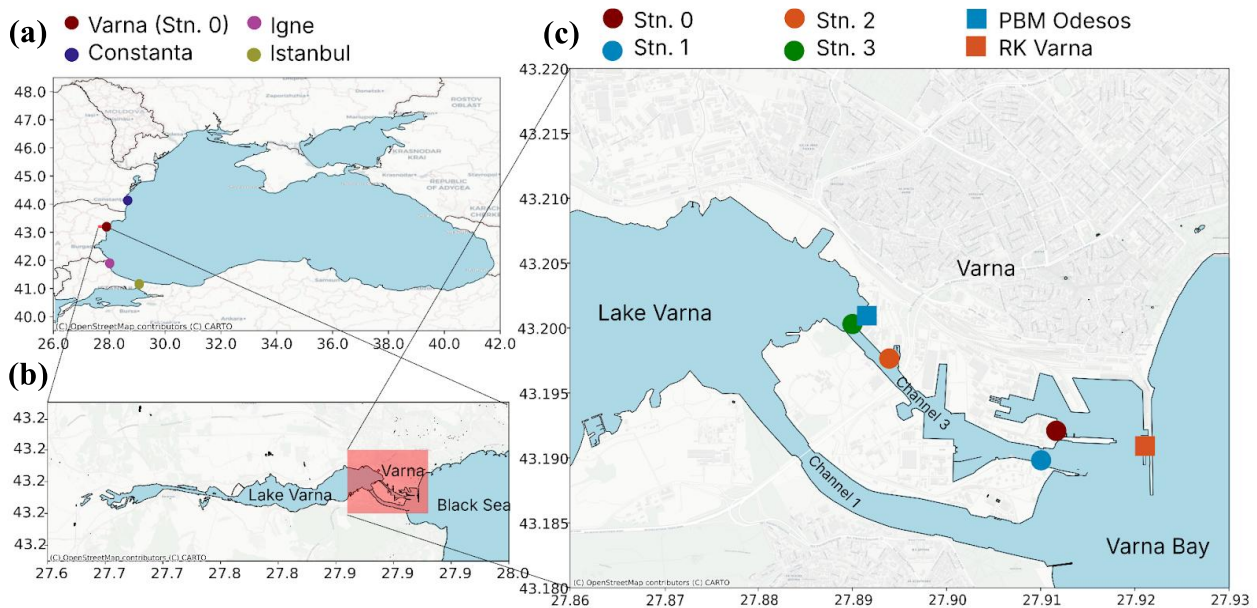


Figure 1. Location of the study area, shown on the map of the Black Sea (a), and the map of the Varna region (b). Detailed map (c) displays the locations of the observation sites. The Black Sea map (a) presents the western coastal stations where data are shared within the Copernicus Marine Service <https://marine.copernicus.eu/>.

105 2.2 Observations

The experimental setup involved installing flow measurement devices, called Hydromasts (Egerer et al., 2024), at three locations in the port area, with the measurement sites shown in Fig. 1 and exact data presented in Table 1. The Hydromast is a flow-monitoring device that uses a 3D Hall-effect sensor to measure direction and velocity. In addition, it is equipped with absolute pressure and temperature sensors. These devices have been shown to provide accurate measurements across various marine applications (Egerer et al., 2025; Eelsalu et al., 2025).

110 Measurement locations were chosen to avoid interfering with port activities and to minimize the risk of damage. Station 1 (labeled Stn. 1) was positioned near the sea boundary of the Port of Varna channel, under a floating dock, allowing flow measurements with minimal obstructions. Station 2 (Stn. 2) was in the middle of the narrow port channel connecting the Black Sea's Varna Bay to Varna Lake, and Station 3 (Stn. 3) was next to the lake boundary of the channel. At Stn. 1, the



115 installation is in a free-flow area, whereas at Stn. 2 and Stn. 3, the sensors are installed next to a concrete pier protruding about 40 cm from the pier. All sensors were placed 0.5 m above the bottom at depths of approximately 3.5 m.

Water level data were also obtained from the near-real-time (NRT) in situ quality-controlled Copernicus Marine service. In the study area, the “Varna station” of the Black Sea in situ network provided standard hourly observations; upon request, 1-minute-resolution data were also obtained at a location labeled Stn. 0. Meteorological data (wind speed and direction, atmospheric temperature, and pressure) were obtained with a resolution of 10 minutes from the Port Varna meteorological stations, RK Varna and PBM Odesos, as shown in Fig 1.

The experimental period started on 18 February 2025, when stations 1 and 2 came online, followed by Stn. 3 on 6 March 2025 (Table 1). Although the data collection period for different sensors was longer across all three datasets, this paper considers the three months from 18 February to 18 May 2025, as this period coincides with the continuous measurement period across all devices.

Table 1. List of observation points and data availability for the experimental period starting from 18 February 2025.

Station	Coordinates	Data log start	Data log end	Comments
Stn. 0	43.1920 N 27.9110 E	Not applicable	Not applicable	Water level, a mareograph station by the Bulgarian authorities
Stn. 1	43.1897 N 27.9101 E	18.02.2025 12:00	17.07.2025 23:59	Currents and water level, installed during the experiment
Stn. 2	43.1977 N 27.8934 E	18.02.2025 11:00	16.07.2025 23:59	Currents and water level, installed during the experiment
Stn. 3	43.2004 N 27.8898 E	06.03.2025 00:00	23.06.2025 11:59	Currents and water level, installed during the experiment
PBM Odesos	43.2006 N 27.8902 E	Not applicable	Not applicable	Meteorology, a weather station by the Bulgarian authorities
RK Varna	43.1926 N 27.9211 E	Not applicable	Not applicable	Meteorology, a weather station by the Bulgarian authorities

The Hydromast records all data at 50 Hz. The collected raw data is processed following Egerer et al. (2024) to get velocity and direction estimates. The Hydromast devices with a mast length of 500 mm were used at all three sites, providing reliable velocity estimates ranging from 0.06 m s⁻¹ to 0.6 m s⁻¹. For this work, the data is downsampled to 0.0166 Hz (1 minute).

The pressure logger records absolute pressure. The absolute pressure readings are corrected for atmospheric pressure using the RK Varna and PBS Odesos weather stations at the Varna port. In addition, correction with respect to the temperature is done using the following equation:



$$P_{hm} = [P_{hm0} - (aT_{hm} + b)] - P_{ref} , \quad (1)$$

where T_{hm} is the temperature reading for the Hydromast in the water, a and b are empirically determined constants, and P_{ref} is a pressure sensor bias value ensuring that in air at the same temperature, P_{hm} and atmospheric pressure P_{atm} are equal.

140 2.3 Analysis methods

The one-minute average velocity, water column height, and direction were calculated by grouping the data into 1-minute bins and computing the arithmetic means for each bin. The false data recordings, identified by data quality assurance filters, were removed and replaced with NaN (Not a Number) values for further analysis. Shorter-scale processes lasting less than one minute were not considered relevant to this study.

145 To find the dominant oscillation frequency in the channel, the power spectral density (PSD) was calculated using the Welch method. The main analysis was performed using a window length of 10 days (14,400 minutes) and a window overlap of 5 days (7,200 minutes) for all 4 stations (3 Hydromast and 1 Copernicus). The large window length was chosen to ensure the diurnal and semidiurnal cycles are included. However, given the extended duration and broad range of periodicities of interest, we tested multiple segment lengths and overlap parameters to evaluate the sensitivity of spectral features to analysis settings. For each configuration, the time series was partitioned into overlapping windows, and each window was tapered with an appropriate window function. Only those frequency peaks that consistently appeared across varying window sizes and overlap choices were retained for further analysis. This procedure ensures that detected spectral features are not artifacts of specific parameter settings. Furthermore, we required that consistent peaks be present across all measurement sites before inclusion in the final interpretation. In addition, a comparison between pairs of stations in the frequency domain was
150 performed using coherence analysis. The comparison included coherence calculations between all stations using 5-day segments and a 2-day overlap.

Consideration of sub-hourly data revealed events of increased variability of currents and water level, which will be identified in sub-section 3.2 and analyzed in 3.4. A monthly spectrogram covering the dominating events was generated. Furthermore, wavelet analysis was performed on the high-current-speed events. Wavelet transforms decompose a signal into
160 components representing different frequency bands while preserving temporal localization, making them suitable for analyzing non-stationary signals whose frequency content varies over time. As the data span long periods and our interest includes high-frequency components during shorter events, we applied the discrete wavelet transform using the Daubechies wavelet (db4). This analysis examined how dominant frequency components evolve and identified frequency bands present at multiple measurement stations along the channel. To quantify the similarity of two selected water level signals at different
165 frequency bands, the cosine correlation of wavelet coefficients was calculated across corresponding decomposition levels.



3 Results

3.1 Observed meteorological, water level, and current time series

The analyzed period of observations spanned three months, from the end of winter (18 February 2025) to the end of spring (18 May 2025), during which the mean air pressure was 1016 hPa (min 997, max 1038 hPa), equal to the long-term spring average. Mean wind speed was 4 m s^{-1} as usual for the region; its instantaneous maximum amounted to 20 m s^{-1} . The mean wind vector was 0.62 m s^{-1} directed to the west-southwest.

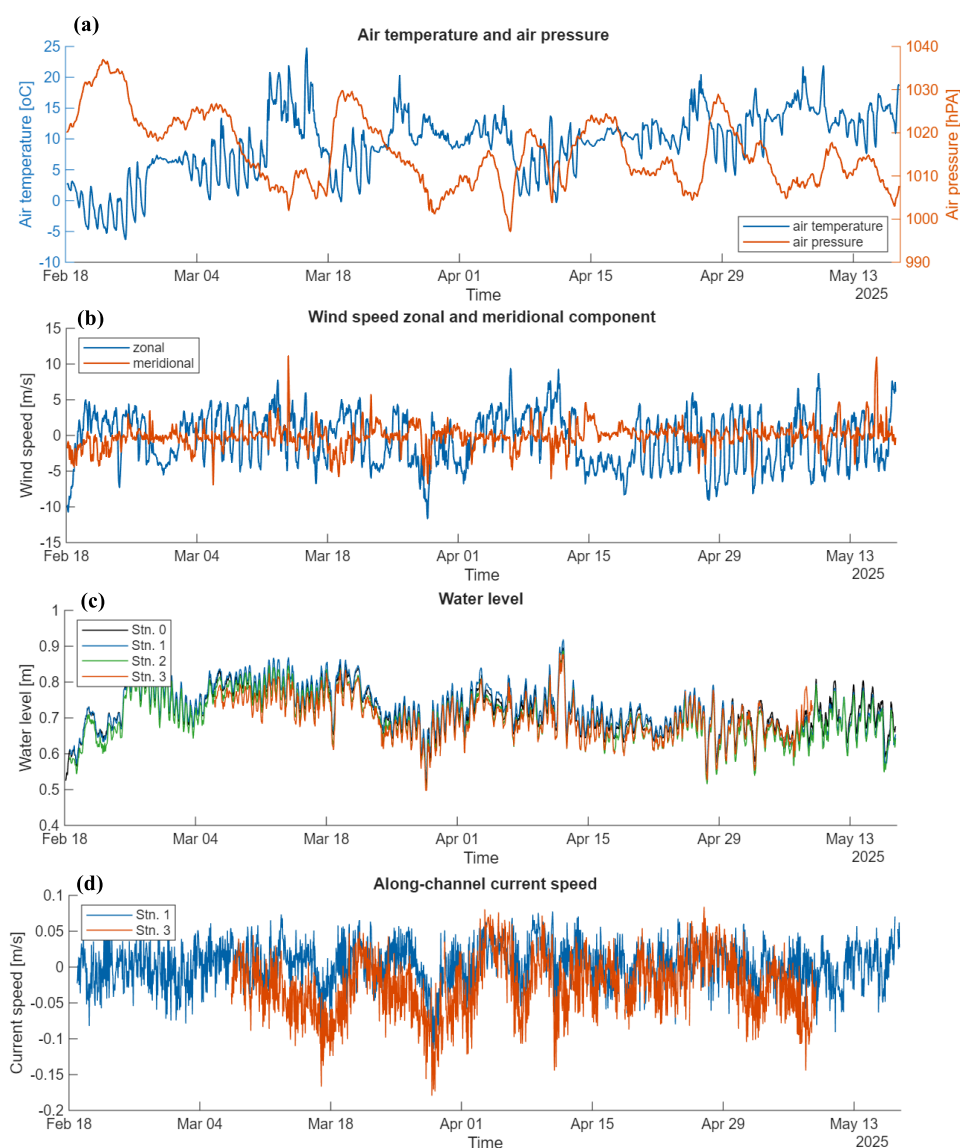


Figure 2. Time series of meteorological and oceanographic data with 1-hour resolution: air temperature and air pressure (a), zonal and meridional components of wind speed (b), water level (c) and along-channel current speed (d) at stations from Stn. 0 to Stn. 3.



175 In this sub-section, we consider variability based on hourly time series, filtered from the original, higher-resolution data using the Tuckey filter with a 2 h length (Fig. 2). Hourly resolution is also widespread in the dissemination of metocean observation and forecast data. We note that the variance of hourly changes in wind and water level exceeded 80% of the total variance, including the high-resolution sub-hourly data. In the time series of currents, hourly changes covered only 30% of the total variance.

180 Air temperature (Fig. 2a) generally reflected seasonal warming, ranging from -5 to +20 °C. Still, the weekly course depended on weather patterns over the area. High-temperature events above +20 °C were observed as early as the middle of March, during relatively low air pressure (Fig. 2a) and the strongest southerly winds (Fig. 2b).

Strong diurnal variations in temperature and the zonal (cross-shore) wind component developed during periods of stable air pressure, with temperature amplitudes up to 10 °C and zonal wind component amplitudes up to 10 m s⁻¹. Over the whole study period, deviations from daily mean zonal temperature and air temperature remained uncorrelated. During the seasonal warming period, from 20 April to 18 May, their correlation was 0.62. Nightly lower temperatures at the Varna meteorological station were associated with a land breeze (an offshore wind). Daytime faster heating over land, compared to that over the sea, corresponded to sea breeze (onshore wind). Therefore, differences in diurnal heat cycles over land and sea result in a drop in air temperature and associated winds (Abbs and Physick, 1992). Such breeze events were studied on the Bulgarian coast by Barantiev et al. (2011). The breeze caused an imprint on the water-level variations as well. Starting 27 April, usual semidiurnal oscillations at all four observation sites were suppressed, and diurnal oscillations became dominant (Fig. 2c), with daily extreme water levels observed during minimal zonal wind.

195 Water level variations occurred on top of the average sea level. Mean sea levels at Stn. 1 and Stn. 3 were 0.727 m and 0.700 m, respectively, with the difference being within datum uncertainty. Water level variability during the study period, including the semidiurnal and diurnal oscillations noted above, was characterized by a standard deviation. It was 0.064 m in the seaside location and decreased to 0.058 m near the lake. The hourly water-level changes at all four stations were highly correlated, with Pearson correlation coefficient $r > 0.96$.

The lowest hourly water level (0.50 m; Fig. 2c) was observed on 28 March. This low-water-level event is explained by the strongest winds, up to 20 m s⁻¹, blowing onshore from the east and northeast. Another local water-level minimum of 0.61 m was observed on 18 March; it has no obvious link to local wind forcing. The highest water level of 0.91 m was observed on 12 April, when westerly onshore winds of about 10 m s⁻¹ turned to northerly winds. The water-level minima and maxima in Varna were consistent with those at the standard coastal station in Istanbul, located 250 km away (data distributed by the Copernicus Marine Service), indicating the influence of large-scale atmospheric forcing over the Black Sea.

205 Currents at Stn. 1 and Stn. 3 were constrained by the flow mainly oriented along the channel. Near the seashore, at Stn. 1, 38% of the time the currents had a direction around 110° (±30°) and 25% around 310°. At Stn. 3 near the lake, the directions around 190° covered 40% of the time, and 34% around 310°. The alongshore currents (Fig. 2d), aligned at 20° at Stn. 1 and 40° at Stn. 3, were rather well correlated, with a Pearson correlation coefficient $r \approx 0.67$. Both low-water-level events on 17-18 March and 28 March were associated with landward (negative) along-channel hourly flows up to 0.17 m s⁻¹.



At the lakeside Stn. 3, the landward current speed was about 0.04 m s^{-1} larger than at the seaside Stn. 1. Regarding hourly
210 scalar current speeds, events of higher current speed (up to 0.25 m s^{-1}) were observed coherently at both stations on around
17 and 28 March, and 7 and 11 April, in association with higher wind speeds (Fig. 2b).

In this subsection, we identified the episodes of high hourly current velocity that were synchronous along the channel.
Our unique study, which uses 1-minute resolution current and water-level observations, enables detailed analysis of sub-
hourly oscillations. These findings will be presented in the next sub-sections.

215 3.2 Sub-hourly variability

Instantaneous 1-minute time series of currents and water levels had a larger variation range than hourly data. Current speed
amounted to 0.75 m s^{-1} , compared to 0.25 m s^{-1} in hourly data. The water level range was $0.27\text{--}1.16 \text{ m}$, compared to 0.50--
 0.91 m for the hourly data. The largest changes were found at Stn. 1 in the seaside part of the channel.

Intensity of sub-hourly variations is described by the standard deviation of sub-hourly values over one-hour intervals
220 (Fig. 3). The sub-hourly intensity of scalar current speed and water level had a background of 0.03 m s^{-1} and 0.03 m ,
respectively (Fig. 3a). Notably, high-amplitude events were observed on 16-18 March and on 28-29 March 2025 when a 5-
fold increase from the background was found.

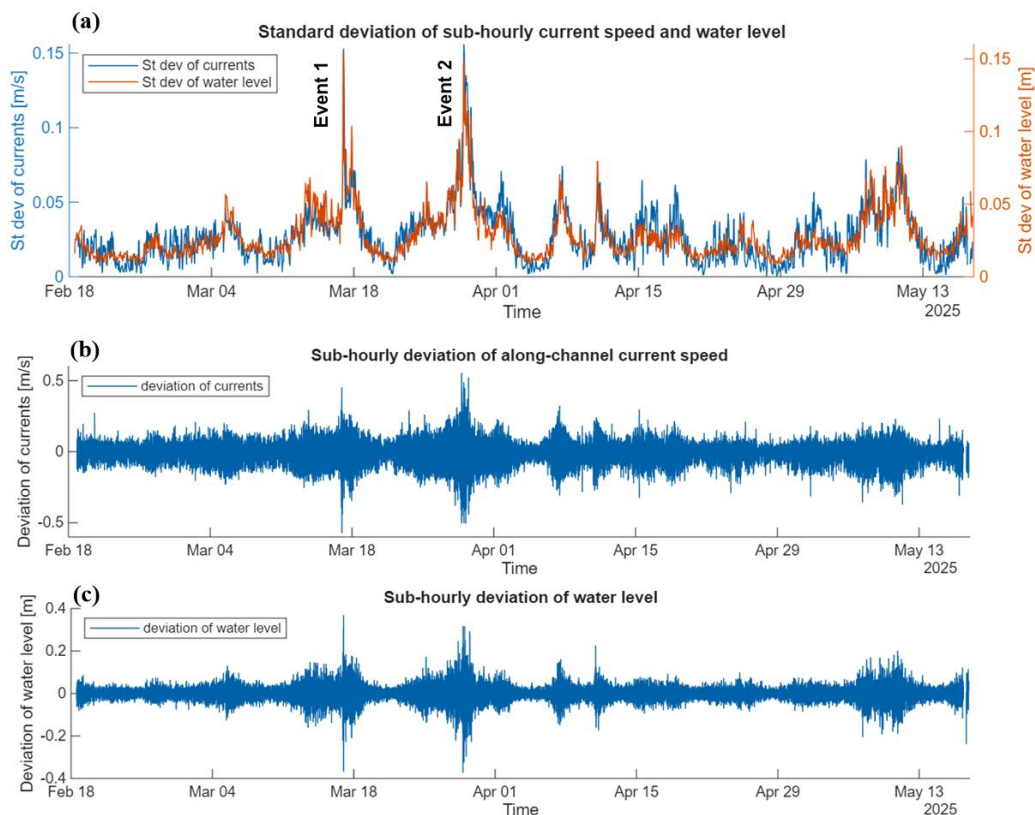
The most intense high-current-speed events, described above, are labeled Event 1 and Event 2 (Fig. 3). Several smaller
events occurred, including those on 7 and 11 April.

225 The sub-hourly water level deviations from their low-passed counterparts had gradually decreasing correlation from sea
towards lake: correlation with seaward Stn. 0 decreased from $r = 0.74$ for seaside Stn. 1 to $r = 0.21$ for lakeside Stn. 3.
While the 1-min-resolution currents at Stn. 1 and St. 3 were uncorrelated, their hourly standard deviations were strongly
correlated with $r = 0.87$.

230 Considering the typical time scale of 10 min for sub-hourly oscillations, given in Fig. 3b, c, the maximum changes in
current and sea level - up to 0.8 m s^{-1} and 0.8 m , respectively - are harmful to ship navigation, harbor operations, and coastal
management.

3.3 Oscillatory analysis

Water level oscillations in the channel were studied using spectral analysis (Fig. 4) and coherence analysis (Fig. 5). Spectral
analysis was performed using the Welch method to estimate the power spectral density over a specified frequency range. The
235 basic analysis over a broad frequency range corresponding to periods from 6 min to 14.5 h (subsection 2.3) revealed that the
semidiurnal peak (period about 12 h) had the highest amplitude. This oscillation period is dominant over the whole Black
Sea (Medvedev and Kulikov, 2016; Medvedev, 2022) due to tidal forcing. Note that historical spectral estimates lack the
high-frequency part of the spectrum due to the 1-hour interval of the available observational data.



240

Figure 3. Joint panel of sub-hourly standard deviations of current speed and water level over one-hour period (a), and the time series of 1-minute resolution sub-hourly deviations of along-channel current speed (b) and water level (c). Labeled are the high-speed cases Event 1 and Event 2.

Fourteen spectral peaks, P1-P14, have been identified in the 3-month dataset using the objective procedure described in subsection 2.3. In contrast, frequency components that were consistently observed across varying Welch window and overlap settings and present at all measurement sites were retained. They are presented in Table 2 and marked in Fig. 4. Among the 14 peaks, determination of 12 longer periods is robust, but 2 shorter periods were somewhat more uncertain, depending on the selection of the calculation window. Most of the frequency peaks were “flat” in space, with the spectral peaks at four locations being nearly equal. Such flat spectral peaks occurred at longer periods, from 12 h (P1) to 4.2 h (P3), at 92 min (P6), at 37 min (P9), and at the shorter periods 24 and 19 min (P11 and P12). Coherence analysis (Fig. 5) revealed high levels for all the identified spectral peaks, meaning nearly synchronous oscillations along the channel. Coherence reduction was evident between the sea-dominant peaks P5 (141 min) and P8 (52 min), but it peaked high again at the flat modes of 92 min (P6) and 66 min (P7). In the shorter periods, reduced coherence became evident between the flat 37 min (P9) and sea-dominant 27 min (P10) modes.

255

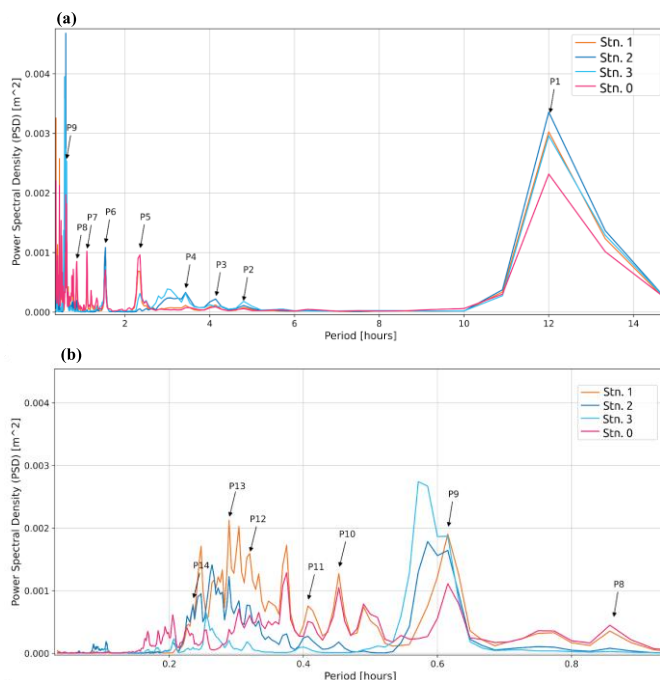


Figure 4. Power spectral density of water level at the four measurement sites of the channel in the range of periods from 2 min to 15 h (a) and zoomed curves with periods up to 1 h (b). Marked are the peak periods, starting from the longest period, P1, to the shortest period, P14. Main features of the oscillation peaks are given in Table 2.

260 Further insight into the time-dependent character of oscillation amplitudes was gained through spectrogram analysis at Stn. 1 (Fig. 6), which used the short-time Fourier transform (STFT) with a 12 h window and 6 h overlap over successive segments. In the nearly monthly spectrogram, sub-hourly oscillations were concentrated at periods of 36 min and 16–17 min (slightly variable in time), corresponding to the peaks P9 and P12–P13 in the 3-month spectra. The oscillations were amplified on 17 and 29 March. These intervals were noted earlier as Event 1 and Event 2 (subchapter 3.2), based on the
 265 descriptive graphs of sub-hourly variability (Fig. 3).

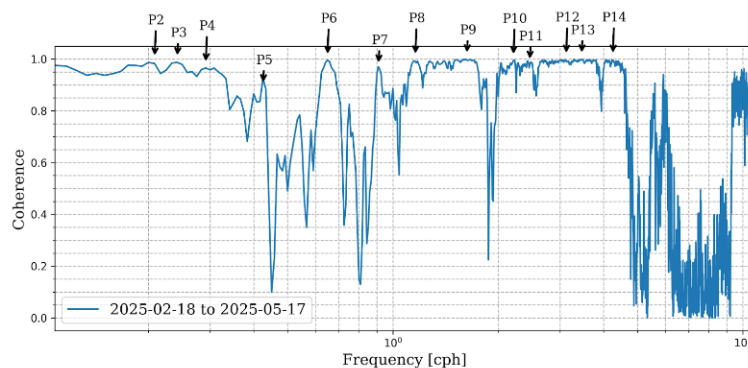


Figure 5. Coherence of water level variability in the channel between Stn. 1 and Stn. 3. The frequency band is from 0.1 to 10 cph (cycle per hour). Marked are the spectral peaks from P2 to P14 shown in Fig. 4.



270 **Table 2. Summary of the spectral analysis of water level time series, with properties of 14 identified spectral peaks. The spectral peaks (given by frequency and period) are characterized by average and maximum intensities in dB and by coherence between Stn. 1 and Stn. 3.**

Peak	Freq [cph]	Period [minutes]	Average intensity (dB)	Max	Coherence Stn. 1, Stn. 3	Notes on along-channel structure
P1	0.08	720	21.03	143.65	0.995	Flat, 12 h semidiurnal
P2	0.21	287	2.54	2.79	0.924	Flat
P3	0.24	249	3.09	3.64	0.932	Flat
P4	0.29	206	7.17	10.13	0.944	Lake dominant
P5	0.43	141	8.00	10.13	0.928	Sea dominant
P6	0.65	92	7.35	8.10	0.985	Flat
P7	0.91	66	6.70	8.10	0.302	Sea dominant
P8	1.16	52	6.50	7.37	0.844	Sea dominant
P9	1.63	37	6.04	6.04	0.978	Flat
P10	2.21	27	3.86	5.64	0.287	Sea dominant
P11	2.46	24	3.41	5.64	0.811	Flat
P12	3.12	19	0.49	1.27	0.830	Flat
P13	3.46	17	0.49	1.27	0.951	Sensitive to window selection
P14	4.25	14	-2.32	0.65	0.850	Sensitive to window selection

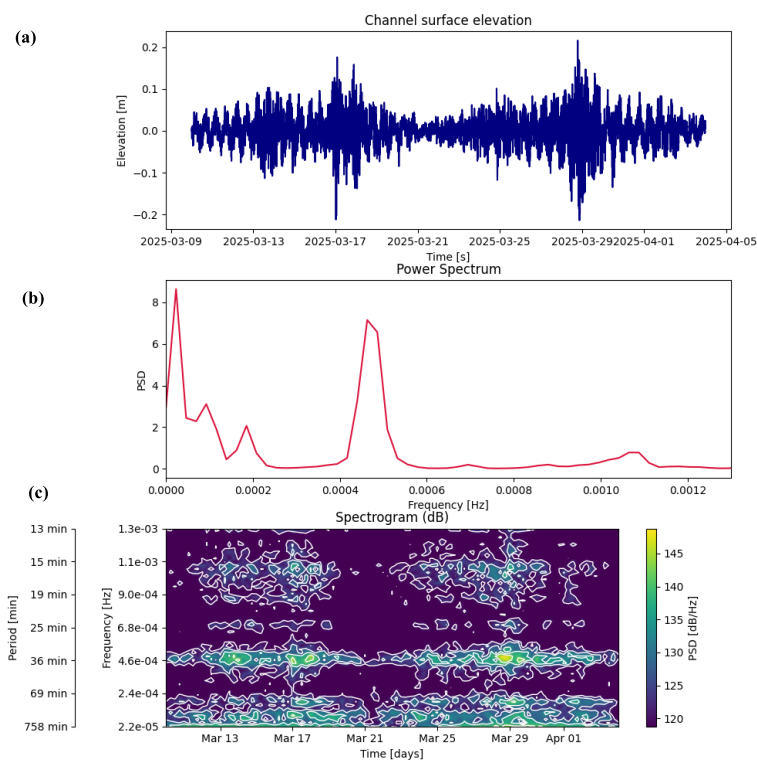
275 The identified 12 “robust” oscillatory peaks P1–P12 and their spatial patterns - flat in four observation stations (7 peaks), sea dominant (4), and lake dominant (1) - will be further analyzed in subsection 3.5 by interpreting the dominant oscillation patterns using the seiche concept, relying on the theory and model of barotropic long waves in the channel.

3.4 Analysis of high current speed events

280 The Events 1 and 2 of high-amplitude water level and current oscillations are visualized by twelve-hour snapshots shown in Figs. 7 and 8, respectively. Correlation of 721 values of 1-min water levels had rather high values of 0.87 inside the channel between Stn. 1 and Stn. 2 for both events; it reduced to 0.53 and 0.61 between seaside and lakeside stations Stn. 1 and Stn. 3, for Events 1 and 2, respectively. The mean periods of most intensive oscillations, measured between sequential maxima and minima, were 18 min and 27–40 min for Event 1, and 33–37 min and 15–17 min for Event 2. These periods agree with the results from the spectrogram (Fig. 6).



Event 1 was characterized by decreasing westward winds within a diurnal breeze cycle. A short pulse of strong southerly wind occurred 4 days before the event. Just before the highest water level, the zonal wind had a 2-h variation (between consecutive maxima) with an amplitude of 8 m s^{-1} . Shorter period wind speed oscillations were rather weak, less than 1 m s^{-1} . During Event 2, the zonal wind had a westward component with a maximum of -14 m s^{-1} ; superimposed variations of 4 m s^{-1} amplitude had a time scale from 50 to 80 min, shorter-period wind pulsations of 2 m s^{-1} had a time scale of about 20 min, close to the period of sub-hourly water level oscillations.



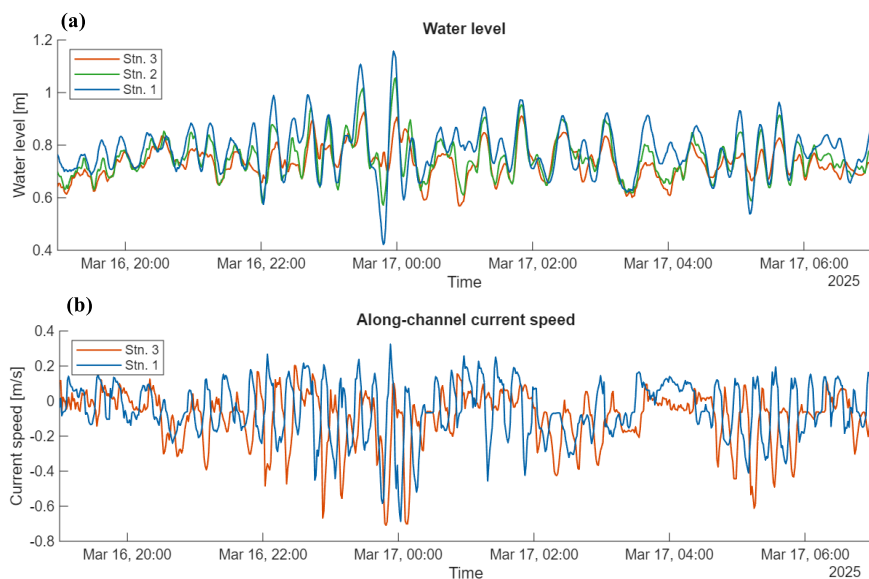
290 **Figure 6.** Water level variability at Stn. 1 from 9 March to 5 April 2025 with a 12 h window and 6 h overlap over successive segments. The original data (a), integrated power spectrum (b), and the frequency vs time spectrogram (c).

During Event 2, wind was variable on a time scale of a few tens of minutes. At the near-lake Stn. 3, water level oscillations were mostly of a 36 min period but were slightly modulated by about a 17-min period. After the peak water level at seaside Stn. 1, the periods changed from 36 min to 16–17 min. In Event 1, which had a 2-h zonal wind variation before the water-level maximum, the periods increased from shorter to longer values.

Signal delay from the sea towards the lake was detected in several instances, but statistically, the best correlation for both events was obtained with zero time lag. There was a smaller correlation decay in the case of signal propagation from the sea towards the lake, in comparison to the opposite direction. Event 1 had a more compact water-level maxima pattern than Event 2; it had 8 versus 14 higher local maxima, measured by the 80% value of the event maximum. Also, the water level standard deviation of Event 1 was about 20% smaller than that of Event 2.

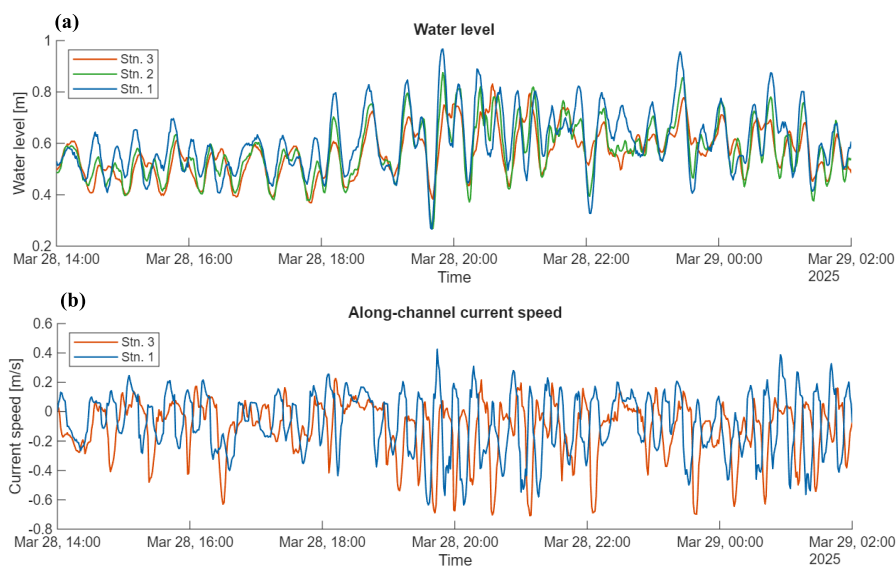


Along-channel currents of Stn. 1 and Stn. 3 are presented in Fig. 7b and 8b for Events 1 and 2, respectively. In many cases, the current fluctuations at seaside and lakeside locations are out of phase. The current time series, unshifted in time, were uncorrelated in both events; a moderate correlation (0.5–0.6) was observed for time shifts of 16–17 min.



305

Figure 7. Water level (a) and along-channel current speed (b) during 12 hours of the high-current-speed event on 16–17 March 2025. Initial data with a 1-minute resolution.

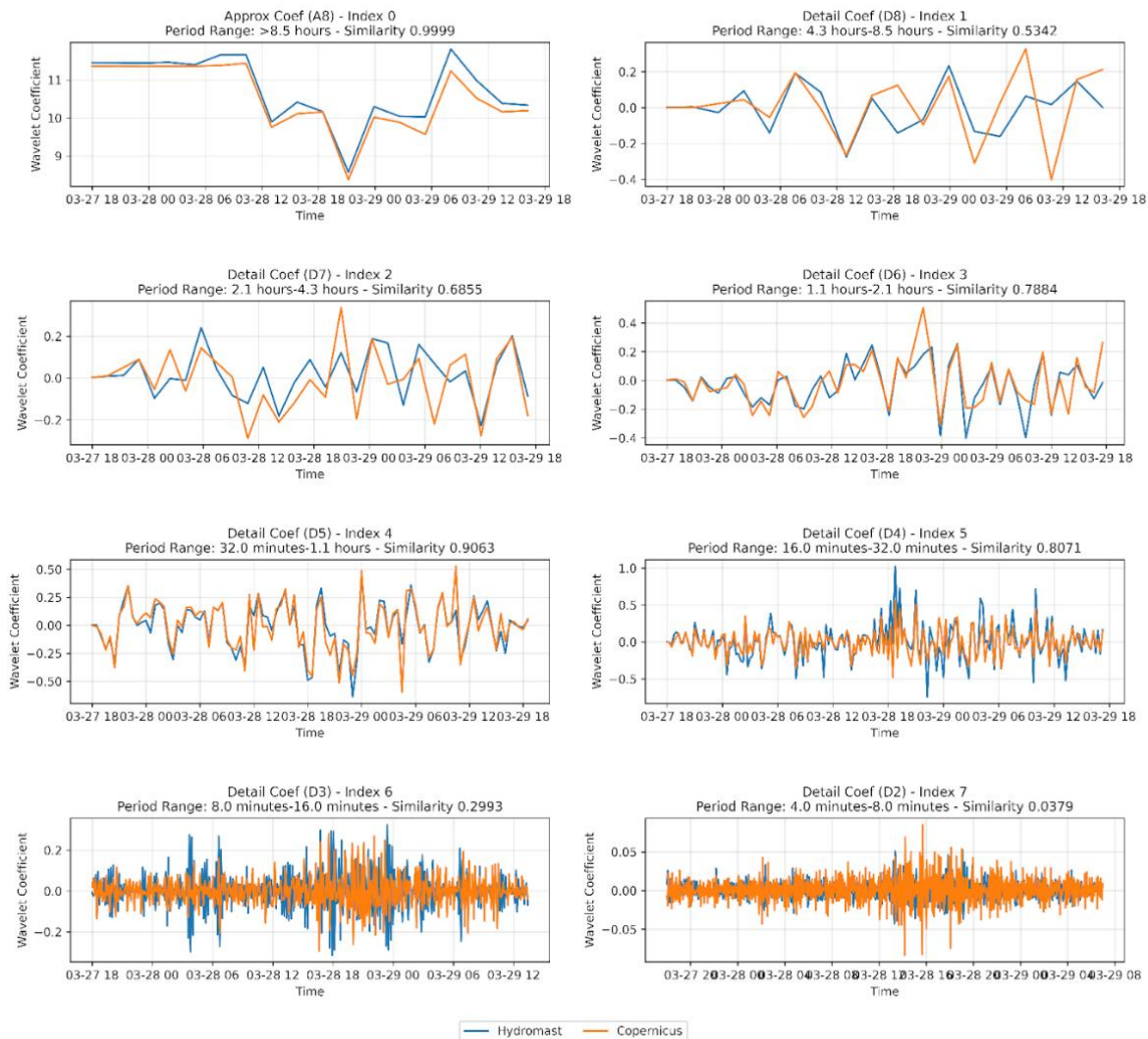


310

Figure 8. Water level (a) and along-channel current speed (b) during 12 hours of the high-current-speed event on 28–29 March 2025. Initial data with a 1-minute resolution.



Wavelet analysis was also applied to study water-level oscillations at both events. The wavelet components in different frequency bands are presented in Fig. 9 for the seaward harbor site Stn. 0 and the seaside channel site Stn. 1. Correlations (similarities) between the wavelet component time series of Stn. 0 and all the other three observation sites are summarized in Table 3. At longer periods (more than 8.5 h), all the channel observations showed high similarity (correlation of 0.99) with the data from Stn. 0. The seaside Stn. 1 had high similarity with outside Varna observations at Stn. 0, also in the shorter periods down to 16 min, for both events. The shorter periods from 16 min to 1.1 h covered the resonance periods of long barotropic gravitational waves in a system of a sea-channel-lake (see the next subchapter). At these periods, a higher similarity with Stn. 0 also occurred at Stn. 2, located in the middle of the channel.



320 **Figure 9.** Anatomy of the high-current-speed event from 27 to 29 March, based on 8 frequency bands shown in the sub-figure headings, identified by wavelet analysis. Comparison between Stn. 0 and Stn. 1.



Based on the above, Event 1 involved a few high-peak 16–17-min oscillations, observed within about an hour, not directly related to the local meteorological forcing. Such a short pulse is typical of meteotsunamis (Vilibić et al., 2021). Event 2 had a longer duration, involving several oscillations, including also longer 36-min period oscillations, likely generated by short-period (including sub-hourly) meteorological forcing.

Table 3. Cosine similarity (correlation) of the wavelet amplitudes at Stn. 1 to Stn. 3 with Stn. 0 at different intervals of periods during Event 1 and Event 2.

Interval of periods		Event 1, 16–18 March 2025			Event 2, 28–29 March 2025		
from	to	Stn. 1	Stn. 2	Stn. 3	Stn. 1	Stn. 2	Stn. 3
long	8.5 h	0.99	0.99	0.99	0.99	0.99	0.99
4.3 h	8.5 h	0.64	0.32	0.28	0.53	0.25	0.23
2.1 h	4.3 h	0.73	-0.15	-0.18	0.69	0.49	0.35
1.1 h	2.1 h	0.83	0.45	0.35	0.79	0.27	0.09
32 min	1.1 h	0.78	0.61	0.47	0.91	0.55	0.31
16 min	32 min	0.7	0.52	0.25	0.81	0.58	0.22
8 min	16 min	0.27	-0.06	-0.31	0.3	0.02	-0.22
4 min	8 min	-0.03	-0.09	-0.24	0.04	-0.2	-0.32

3.5 Interpretation of variability by long barotropic waves

The dynamics of channels and their networks are frequently treated using shallow-water theory, which considers along-channel flow variations averaged over depth and width and employs conservation laws for mass, momentum, and energy in the form of differential equations. A broad spectrum of problems includes flooding and flow routing, long-wave dynamics for transient waves, their reflection, transition, and damping depending on the degree of nonlinearity (e.g., Lighthill and Whitham, 1955). Adopting from the observations the water-level amplitude up to 0.4 m and current-velocity amplitude up to 0.4 m s⁻¹ over a half-period of 10 min, the flow is mostly in a linear regime, since in the momentum equation, non-linear advection is less than 10% of the acceleration term. The linear barotropic (density variations are considered small) shallow-water equations (Eq. A1) and related oscillation modes are outlined in the Appendix.

The study area was idealized using a connected, rectangular-basin approach, assuming constant depth and width within each basin. The navigation channels were approximated with length $L = 2,400$ m, depth $H = 7$ m, and width $B = 300$ m; the lake was approximated with length $L = 11,000$ m, depth $H = 10$ m, and width $B = 1,900$ m. The two channels (Channels 1 and 3), approximately the same length and depth, were merged into a single channel by summing their widths.



Seiche (standing wave) periods were studied using analytical and numerical experiments, labeled from Exp. 1 to Exp. 7 (Table 4). Already, the simplest model approaches of Exp. 1 and 2 revealed an approximate match to the range of observed oscillation periods of a few tens of minutes (Table 2). Further refinements from Exp. 3 to Exp. 7 included different configurations of the connected sea, channels, and lake, using analytical and numerical methods.

Table 4. Periods of eigenoscillations (seiche) of the first 5 modes, based on 7 experiments with different models, number of included basins, and type of basin geometry. For comparison, observational peak periods P4, P9, and P12 are taken from Table 2.

Mode number				0	1	2	3	4	5
Exp.	Type of model	No. of basins	Type of geometry	Oscillation period (min)					
1	Analytical	1	Channel only	19.3	6.4	3.9			
2	Analytical	1	Lake only	74.0	24.7	14.8	10.6		
3	Analytical	1	Channel and lake, equal depth, length summed	97.4	32.5	19.5	13.9	10.8	8.9
4	Analytical	2	Equal width of channel and lake, different depths	98.2	32.7	19.6	14.0	10.9	8.9
5	Analytical	2	Different depths and widths of the channel and the lake	195.9	36.1	18.7	13.0	11.5	9.2
6	Numerical	2	Different depths and widths of the channel and the lake	196.0	36.1	18.6	13.0	11.4	9.2
7	Numerical	3	Sea basin added before channel, different depths and widths	184.6	35.8	18.5	12.6	10.5	9.1
	Present observations (Table 2)		Peak number period (min)	P4	P9	P12			
				206	37	19			

Analytical treatment (from Exp. 1 to Exp. 5) of shallow water equations includes, as a special case, the spatial modes (oscillation patterns) depending on the applied boundary conditions. When outer-basin water-level oscillations drive the water level in a channel, the appropriate condition for calculating the spatial modes is to impose a zero water level at the open boundary. The other boundary is considered closed, which makes the velocity zero, equivalent to setting the spatial gradient of the water level to zero. When the basin is “clued” from different parts, with different depths, lengths, and widths, conditions of continuity are applied at the connection point. In the simplest case of one basin of constant depth and width, the “quarter-wave” modes take place as given by Eq. A2.

Three basic one-basin experiments, Exp. 1 (channel only, forced in the sea, closed at the connection to the lake), Exp. 2 (lake only, forced at the connection to the channel, closed at the western end of the lake, and Exp. 3 (joint channel and lake, mean depth, equal widths, lengths summed) provided self-oscillations (seiche) in the range of periods 13–40 min, involving the observed spectral peaks from 37 min (P9) to 14 min (P14). At Exp. 4 and 5, introducing more details of basin geometries, based on Eq. A3 and A4 did not significantly change the periods of modes from 1 to 5. However, the longest period corresponding to mode 0 became longer, from 98 min in Exp. 3 and 4 to 196 min in Exp. 5, corresponding to the lake-amplified observed peak period P4 of 206 min. These free, frictionless oscillation modes just yield the resonant periods.



When variable forcing by water level and/or wind stress is applied, the amplitude of the response oscillations is maximal (local maximum of the amplification factor) when the period of forcing is close to the resonant period.

Modes of standing waves were further studied using time-stepping numerical calculations with the 1D barotropic numerical model as outlined in the Appendix. The spatial grid step was 12 m in the channel and 30 m in the lake. Both basins used a linear friction coefficient of $R = 10^{-4} \text{ s}^{-1}$. Using Eq. A5, the water-level forcing was provided by prescribed oscillations at the seaside boundary. Numerical experiments Exp. 6 and 7 were run over a sufficiently long period (10–30 days) to achieve the regime of persistent forced oscillations. The calculations were conducted over a range of external oscillation periods from 6 min to 330 min. For each different oscillation period, 1000 calculation cycles were made. The attainment of oscillations in the persistent pattern was determined using cumulative analyses of peak time series at selected locations. “Steady” oscillations were selected by a backward cycle of the peak heights being within 8% difference from the cumulative mean peak height. The resulting amplitudes for each forcing period with unity amplitude were collected. The results are presented in Fig. 10, whereas the numerical values of resonant periods are given in Table 4. The origin of each numerically determined resonant period is determined analytically using the mode numbers.

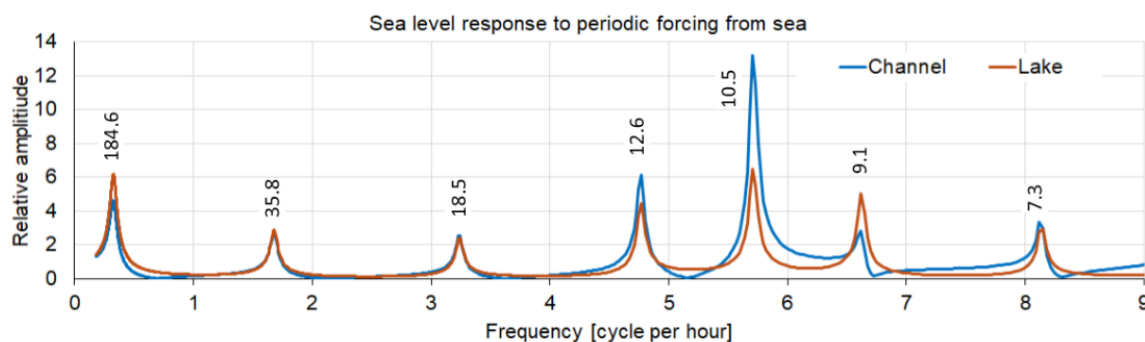


Figure 10. Amplification factor (relative amplitude) of oscillations forced on the seaward side of the channel-lake system with unity amplitude but different periods. Calculations were performed using a numerical model with a linear friction coefficient of $R = 10^{-4} \text{ s}^{-1}$. The resonance periods are 184.6, 35.8, 18.5, 12.6, 10.5, 9.1, and 7.3 min (Table 4, Exp 7).

Observations revealed a sea-dominant peak, P5, at 141 min (Table 2), which was absent from the numerically calculated resonant wave excitation periods (Table 4) but is in good agreement with the resonant frequency of the Helmholtz oscillator (Eq. A6). Note that an equal forcing amplitude was used for all calculated periods due to the lack of high-resolution open-sea data; the observed spectra reflect the actual variability in forcing over the broad range of periods.

The high-amplitude events, presented earlier in subchapter 3.4, do not fit the concept of superposition of standing modes with “saturated” amplitudes. Experiments with forced oscillation patterns in the initial and saturated phases are presented in Fig. 11 over three periods. When forcing starts at the seaside of the channel, part of the signal is reflected at the channel-lake junction. Another part, transferred to the lake, accumulates over time until a stationary oscillation pattern is established throughout the channel-lake system. On the oscillation periods of forcing of 66 min (peak P7 in Table 2) and 24 min (peak P11), the water-level signal was initially confined within the channel. It did not propagate significantly into the

lake, as shown in Figs. 11a and 11b and Figs. 11c and 11d, respectively. The numerical setup was adopted from Exp. 7; these periods were not resonant within the limits of the selected setup. The third selected period, 18 min, corresponds to the observational “flat” peak P12 and mode 2 of Exp. 5–7, developed after initial adjustment into the resonant mode covering both the channel and the lake (Figs. 11e and 11f). Indeed, the pattern in Fig. 11f has two zero crossings, characteristic of the second mode.

395

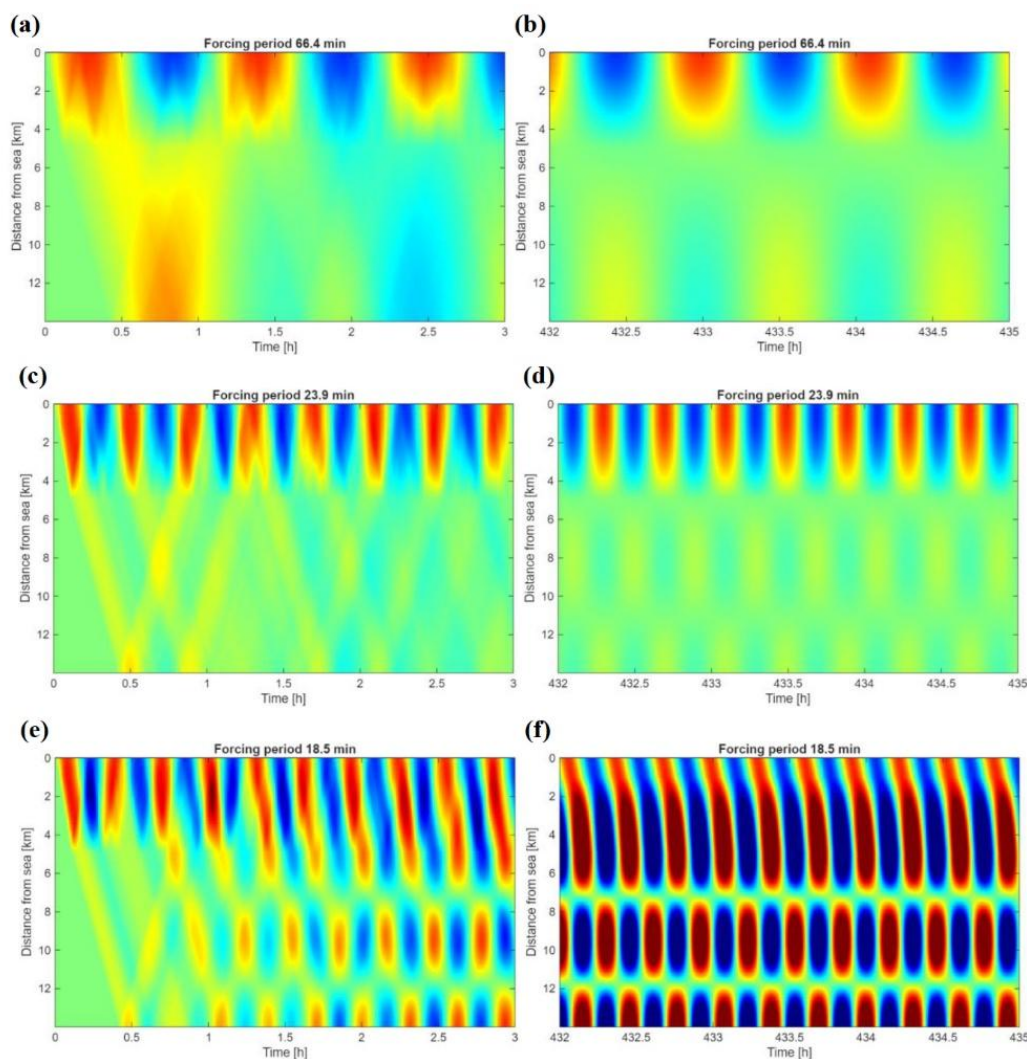


Figure 11. Propagation of sea level oscillations forced on the seaward side of the channel-lake system, with unity amplitude but different periods: 66 min (a, b), 24 min (c, d), and 18.5 min (e, f). Time-distance diagrams cover 3 h during the start of forcing (a, c, e) and during the period of established stationary oscillations (b, d, f). The 300-m-wide channel is changed to a 1900-m-wide lake at the distance of 3 km. The channel has a 600-m-long entrance with a width of 600 m. The color scale “jet” ranges from -1.5 to 1.5.

400

Water level changes in the western Black Sea at the coastal stations of Constanta, Varna (Stn. 0), Igne, and Istanbul (Fig. 1) were well correlated during the study period ($r = 0.7-0.8$) when hourly values from the Copernicus Marine Service



were used. However, using hourly data to drive the channel model yielded smooth variations in water level across the hourly values. Sub-hourly forcing data were not available over the Varna Bay area; therefore, simulation and forecast studies were not conducted.

4 Discussion

4.1 Physics of channel variability

Oscillatory time series from a few points in natural waterbodies are interpreted using wave processes. During resonant forcing of the water level with one or another eigenoscillation period, the initial amplitude growth follows the linear regime used in the present study. In shallow-water Boussinesq equations, at growing amplitudes, non-linear effects, expressed by the cubic non-linearity and quadratic friction, as well as frequency detuning due to finite water-level variation relative to the mean depth, induce slowly evolving subharmonic oscillations of longer periods (Hill, 2003). Assuming the main resonance period in our study was 19 min, the first subharmonic could be 38 min, nearly the same as the observed period. In the pilot study, to interpret the observed sub-hourly water-level and current oscillations, non-linear effects (Teng and Fu, 1992) and variable topography (Valiani and Caleffi, 2024) were not included. For the same reason, full numerical modelling at very high resolution was reserved for future studies.

Sub-hourly current and water-level oscillations have been reported as very important for extreme water levels in the seas with low tidal activity. Recently, Ramos-Alcántara et al. (2025) showed that in the microtidal Mediterranean, sub-hourly periods account for 8–24% of the water-level peak values. At channels and river mouths, this external variability is transferred into coastal embayments, where resonant forcing may occur. In our study, the main limitation was the lack of sub-hourly forcing data for the identified high-current-speed events, driven by resonant sub-hourly sea-level dynamics.

Meteotsunamis, generated by Proudman resonance of weather patterns moving at the speed of long gravity waves, are well distinguishable in microtidal seas like the Mediterranean and Black Sea (Šepić et al., 2015; Vilibić et al., 2021) and the Baltic Sea (Pellika et al., 2022; Nestickeytė et al., 2024). After the forcing event ceases, oscillations usually decay rapidly. In some cases, seiches persist for long periods (Park et al., 2016). Among the resonance drivers, infragravity waves with periods of 0.5–5 min play a role (Gao et al., 2016). In Varna Bay, with depths up to 20 m, the long-wave phase speed reaches 14 m s^{-1} , which is comparable to the typical speed of cold atmospheric fronts. A review of meteotsunami processes is given by Vilibić et al. (2025).

Another possible short-term forcing comes from wind gusts, including sub-hourly intense air pressure and wind perturbations. For example, intensive wind gusts occur during convective thunderstorms (Mohr et al., 2017). Short-term local atmospheric changes occur due to the passage of fronts (Steinheuer et al., 2025).

It is anticipated that Event 1, presented in the Results Chapter, was generated by a meteotsunami, and a rapid change of weather conditions created Event 2.



4.2 Forecasting high current speed events

435 The need for sub-hourly resolution in routine meteorological and oceanographic data was recognized as early as the 1950s
(Van der Hoven, 1957), who showed spectral peaks in wind data at about 1 minute. With the evolution of observation
techniques, high-resolution observations have become more widespread, but the dominant data exchange interval in
meteorology remains 1 hour. In coastal oceanography, water levels are recorded at 1-minute intervals in many locations
since the 1980s (Miller and Luscher, 2019). Presently, there are initiatives to manage high-resolution water level data, such
440 as SHELDA (Sub-hourly European Quality Controlled Sea Level Dataset; Balić and Šepić, 2025), but standard data
exchange for now- and forecasts, such as in Copernicus Marine Service, uses a 1-hour resolution.

The hourly gridded data for the Black Sea, generated with a NEMO v3.4 model at 3 km resolution, are already reliable
(Ciliberti et al., 2022). In another microtidal waterbody, the Baltic Sea, operational sea-level predictions have reached high
performance (Kärnä et al., 2021). Observed sea levels can be extended from the coastal stations to unmonitored coastal
445 and/or offshore locations using the statistical patterns generated from the model results (Elken et al., 2024). Sea level
predictions at coastal sites can be fine-tuned using machine learning (Barzandeh et al., 2025).

Prediction of local dynamics, such as flows and water levels, in the Varna Harbor Channels is a typical “downstream”
forecast problem, and the following steps should be taken.

1. Setting up a specific, very-high-resolution model, probably of a shallow-water Boussinesq-equation model.
- 450 2. Creating a parametrization interface, linking the “core” Black Sea data to the local forcing, with a proper
description of sub-hourly variability. Implementing machine learning might be useful.
3. Conducting an extended observation campaign to calibrate and validate the local model's performance.
4. Running the “downstream” forecast model with a minimum set of observations to fuse the model and observational
data at minimal costs.
- 455 5. Disseminate the forecast data, along with “what-if” guidelines for potential harmful situations.

5 Conclusions

Currents and water levels were studied at 1-minute resolution in the Varna Port navigation channel, which connects the
Black Sea to an upstream lake. While water levels were strongly correlated ($r \sim 0.83\text{--}0.94$) along the 2.4-km-long channel
during a 3-month study period, currents revealed low correlation.

460 Spectral analysis of the water level identified 14 spectral peaks ranging from 14 min to 12 h. Coherence and wavelet
analysis revealed nearly synchronous motions on the periods longer than 14 min; however, coherence was reduced between
some of the observed spectral peaks.

Background sub-hourly variability of currents and water levels, with standard deviations of 0.03 m s^{-1} and 0.03 m ,
respectively, was occasionally interrupted by events of significantly higher variability. Hourly intensity of sub-hourly
465 variations, quantified by standard deviation, showed strong agreement between water levels and currents ($r = 0.86$) along the



channel. The 2-day events revealed dominant oscillation periods of about 19 and 37 minutes, resulting in a 5-fold increase in standard deviation compared to the background.

470 Basic features of high-intensity sub-hourly variations can be interpreted as linear barotropic long waves in a system sea-channel-lake with resonant and damped forcing. The 37-minute oscillations can be explained as the first mode of the channel-lake system. Another period of 19 minutes corresponds to the zero, quarter-wave mode of the channel and the second mode of the channel-lake system.

High current speed events reach 0.8 m s^{-1} in current velocity and 0.8 m in water level for 10 minutes, which is enough to create problems for ship navigation, harbor operations, and environmental protection, especially for coastal management and sediment transport.

475 These high-speed current events can be reliably detected using low-cost observation techniques such as Hydromast, which was used in the present study. Regarding event predictions, the Copernicus Marine Service provides reliable background condition forecasts. The parametrization of the forcing factors for sub-hourly variability – including the effects of meteotsunami generated by moving weather patterns, wind gusts, sub-hourly intense air pressure, and wind perturbations – needs further study to establish their relations with background conditions for the forecast of high-amplitude event
480 occurrence.

Appendix A. Using shallow water equations

Consider long barotropic gravity waves of small amplitude, where the vertical displacement of the water level is much less than the depth of the basin, and the speed of the water particles is significantly lower than the speed of the long waves, within a narrow, elongated basin. The fundamental equations for momentum and volume conservation are outlined in works
485 such as those by Leblond and Mysak (1981) and Cushman-Roisin and Beckers (2011)

$$\frac{\partial u}{\partial t} = -g \frac{\partial \eta}{\partial x} - Ru \quad \text{and} \quad \frac{\partial \eta}{\partial t} = -\frac{\partial}{\partial x}(Hu), \quad (\text{A1})$$

490 where u is the current velocity along the basin, η is the water level elevation, H is the depth of the basin, g is the gravity acceleration, and R is linear friction coefficient.

Adopting constant depth, we may search for the solution in the form $u = u_0 e^{i(kx - \omega t)}$ and $\eta = \eta_0 e^{i(kx - \omega t)}$, where k is the along-basin wave number and the frequency $\omega = \omega_r + i\omega_i$ is complex, where the real part ω_r describes the oscillations and the imaginary part ω_i describes their decay in time. The frequency of oscillations is found from the formula $\omega_r^2 = gHk^2 - R^2/4$. Oscillatory motions are possible when $R < 2ck$, where $c = \sqrt{gH}$ is the phase speed of long gravitational
495 waves without friction.

Assume a semi-enclosed basin of length L , forced by oscillations of the water level of the outer large basin $\eta(0, t) = \eta_0 \sin \omega t$, and closed at the other end $u(L, t) = 0$. For the free, frictionless $R = 0$ modes we use $\eta(0, t) = 0$. The closed



basin end follows the condition $u_n(L, t) = 0$ that becomes equal to $\cos k_n L = 0$ or $k_n = \left(n + \frac{1}{2}\right) \pi / L$. Here n is the mode number of eigenoscillations (seiche mode). Frequencies of all the modes are calculated in the frictionless case in the form

500

$$\omega_n = \frac{\sqrt{gH}}{L} \left(n + \frac{1}{2}\right) \pi . \quad (\text{A2})$$

In the basic mode $n = 0$, a quarter wavelength $\lambda_n = L/4$ interpretation is valid (Leblond and Mysak, 1981), where $\lambda = 2\pi/k$. Then the longest period is $T_0 = 4L/\sqrt{gH}$.

505

Elaborate now the approach to the case of two connected basins with different depth and length, notated by the indexes 1 and 2. The first basin extends in $x \in [0 \dots L_1]$ and the second one $x \in [L_1 \dots (L_1 + L_2)]$. A joint standing wave mode has the same frequency, therefore $k_1 \sqrt{H_1} = k_2 \sqrt{H_2}$. At the connection point of the basins $x = L_1$, there is continuity of water levels $\eta_1(L_1, t) = \eta_2(L_1, t)$ and volume transports $H_1 B_1 u_1(L_1, t) = H_2 B_2 u_2(L_1, t)$, where B_1 and B_2 are the width of the basins. Let us denote $a = \sqrt{H_1/H_2}$ and $b = B_1/B_2$, then after some mathematical transformations, the wavenumber of the joint mode n in the basin 1 is determined from the implicit equation

510

$$k_1 a L_2 + \tan^{-1}[\tan(k_1 L_1)/(ab)] - \left(n + m + \frac{1}{2}\right) \pi = 0, \quad (\text{A3})$$

where the number m is to account for the periodicity of the \tan^{-1} function which is selected for each mode n to yield the last continuous intersection point between the growing values of the \tan^{-1} function and $k_1 L_1$. When $ab \approx 1$, leading to $\tan^{-1}[\tan(k_1 L_1)/(ab)] \approx k_1 L_1$, then the eigenfrequencies are found as

515

$$\omega = \frac{1}{2} \frac{\sqrt{gH_1 H_2}}{L_1 \sqrt{H_2} + L_2 \sqrt{H_1}} \left(n + \frac{1}{2}\right) \pi. \quad (\text{A4})$$

When forcing occurs on the resonant seiche period, then in the frictionless case, the amplitudes go to infinity; therefore, friction must be included in the time-series modelling.

520

To model the dynamics of the coupled elongated basins (sea-channel-lake) with variable time-dependent forcing, we used a traditional option of a 1D numerical model (e.g., Cushman-Roisin and Beckers, 2011). To capture the effects of variable basin width, the continuity equation (the second equation of A1) has been rewritten, reaching the equations

525

$$\frac{\partial u}{\partial t} = -g \frac{\partial \eta}{\partial x} - Ru \quad \text{and} \quad B \frac{\partial \eta}{\partial t} = -\frac{\partial}{\partial x} (BHu). \quad (\text{A5})$$



In addition to the horizontally resolved motions described by the shallow-water equations (A1, A4), an integrated Helmholtz oscillator approach (e.g., Leblond and Mysak, 1981) was used. The basin with a surface area A is connected to the outer sea by a channel which is considered uniform along the axis. Mean water level of the basin is calculated from the volume flow in the channel. The channel flow is driven by a sea-level difference along the channel length between the forcing external water level and the response water level in the basin. The resonant eigenfrequency is given by

$$\omega = \sqrt{\frac{gHB}{AL} - \frac{R^2}{4}}. \quad (\text{A6})$$

535 **Code availability**

The calculations were made using Python and MATLAB programming environments, including the libraries for signal processing. Larger codes were not used.

Data availability

Observational data from Hydromast are openly available in TalTech Data Repository at <https://doi.org/10.48726/86ppj-qfpm96>. In Situ Near Real Time Observations in the Black Sea were provided by the Copernicus Marine Service

Author contribution

MK initiated the method-development observational project, while LP conducted most of the field work and initial data processing. JE joined to interpret oceanographic results. He also took the lead on shaping and writing the manuscript. LP performed major parts of the additional data analysis. All the authors contributed to the discussion and to finalizing the manuscript.

Competing interests

There are no competing interests, as declared by the first author.

Acknowledgements

The authors express their gratitude to Dr Asko Ristolainen for experimental setup design and Mr. Jaan Rebane for the sensor assembly and communications setup. The Port Varna Authorities, Bulgaria, are acknowledged for installing the sensors and providing the weather data

Financial support

The study was conducted within the ILIAD project (grant agreement no. 101037643, EU H2020) and AutoMap Extreme (grant no PSG940, Estonian Research Council). Part of the data processing method development and analysis was co-funded



555 by the European Union and the Estonian Research Council through the TEM-TA38 (Digital Twin of Marine Renewable Energy) project.

References

- Abbs, D.J., and Physick, W.L.: Sea-breeze observations and modelling: a review, *Australian Meteorological Magazine*, 41, 7–19, <https://doi.org/10.1071/ES92031>, 1992.
- 560 Balić, M., and Šepić, J.: SHELDA: Sub-hourly European Quality Controlled Sea Level Dataset, *Earth System Science Data Discussions*, <https://doi.org/10.5194/essd-2025-767>, 2025.
- Barantiev, D., Novitsky, M., and Batchvarova, E.: Meteorological observations of the coastal boundary layer structure at the Bulgarian Black Sea coast, *Adv. Sci. Res.*, 6, 251–259, <https://doi.org/10.5194/asr-6-251-2011>, 2011.
- Catalán, P.A., Cortés, P.I., Sáez, F., Carvajal, M., and Cienfuegos, R.: Toward the classification of bays based on their resonant response to tsunamis, *J. Geophys. Res. Oceans*, 130, e2025JC022446, <https://doi.org/10.1029/2025JC022446>, 2025.
- 565 Barzandeh, A., Ličer, M., Rus, M., Kristan, M., Maljutenko, I., Elken, J., Lagemaa, P., and Uiboupin, R.: Application of the HIDRA2 deep-learning model for sea level forecasting along the Estonian coast of the Baltic Sea, *Ocean Science*, 21, 1315–1327, <https://doi.org/10.5194/os-21-1315-2025>, 2025.
- Cerralbo, P., Grifoll, M., Valle-Levinson, A., and Espino, M.: Tidal transformation and resonance in a short, microtidal Mediterranean estuary (Alfacs Bay in Ebre delta), *Est. Coast. Shelf Sci.*, 145, 57–68, <https://doi.org/10.1016/j.ecss.2014.04.020>, 2014.
- 570 Ciliberti, S.A., Jansen, E., Coppini, G., Peneva, E., Azevedo, D., Causio, S., Stefanizzi, L., Creti, S., Lecci, R., Lima, L., Ilicak, M., Pinardi, N., and Palazov, A.: The Black Sea Physics Analysis and Forecasting System within the Framework of the Copernicus Marine Service, *J. Mar. Sci. Eng.*, 10, <https://doi.org/10.3390/jmse10010048>, 2022.
- 575 Cummins, P.F., Karsten, R.H., and Arbic, B.K.: The Semi-Diurnal Tide in Hudson Strait as a Resonant Channel Oscillation, *Atm.-Ocean*, 48, 163–176, <https://doi.org/10.3137/OC307.2010>, 2010.
- Cushman-Roisin, B., and Beckers, J. M.: *Introduction to Geophysical Fluid Dynamics: Physical and Numerical Aspects*, Cambridge, MA, Academic Press, 875 pp., ISBN 978-0-12-088759-0, 2011.
- Doelman, A., Koenderink, A.F., and Maas, L.R.: Quasi-periodically forced nonlinear Helmholtz oscillators, *Physica D: Nonlinear Phenomena*, 164, 1–27, [https://doi.org/10.1016/S0167-2789\(02\)00361-5](https://doi.org/10.1016/S0167-2789(02)00361-5), 2002.
- 580 Eelsalu, M., Piho, L., Aigars, J., Kelpšaitė-Rimkienė, L., Kondrat, V., Kruusmaa, M., Parnell, K.E., Ristolainen, A., Šakurova, I., Skudra, M., Viška, M., and Soomere, T.: Exponential distribution of wave-driven near-bed water speeds under short-crested waves: a case study in the eastern Gulf of Riga, the Baltic Sea, *Proc. Est. Acad. Sci.*, 74, 23–42, <https://doi.org/10.3176/proc.2025.1.03>, 2025.
- 585 Egerer, M., Piho, L., Zhakanov, B., Kruusmaa, M., Ganchev, T., Stanev, A., Todorov, M., and Ristolainen, A.: Exploring Hydrodynamic Patterns Using the Hydromast: Varna Port Case Study, In *OCEANS 2025 Brest*, IEEE, 1–7, <https://doi.org/10.1109/OCEANS58557.2025.11104387>, 2025.



- Egerer, M., Ristolainen, A., Piho, L., Vihman, L., and Kruusmaa, M.: Hall Effect Sensor-Based Low-Cost Flow Monitoring Device: Design and Validation, *IEEE Sensors Journal*, 24, 5986–5997, <https://doi.org/10.1109/JSEN.2024.3354194>, 2024.
- 590 Elken, J., Barzandeh, A., Maljutenko, I., and Rikka, S.: Reconstruction of Baltic Gridded Sea Levels from Tide Gauge and Altimetry Observations Using Spatiotemporal Statistics from Reanalysis, *Remote Sensing*, 16, <https://doi.org/10.3390/rs16152702>, 2024.
- Gao, J., Ji, C., Gaidai, O., and Liu, Y.: Numerical study of infragravity waves amplification during harbor resonance. *Ocean Eng.*, 116, 90–100, <https://doi.org/10.1016/j.oceaneng.2016.02.032>, 2016.
- 595 Giese, G.S., and Chapman, D.C.: Coastal seiches, *Oceanus*, 36, 38–46, 1993.
- Hill, D.F.: Transient and steady-state amplitudes of forced waves in rectangular basins, *Phys. Fluids*, 15, 1576–1587, <https://doi.org/10.1063/1.1569917>, 2003.
- Kanarik, H., Tuomi, L., Alenius, P., Miettunen, E., Johansson, M., Roine, T., Westerlund, A., and Kahma, K.K.: Currents and their drivers in the Archipelago Sea: insights from ADCP measurements, *Ocean Sci.*, 21, 2125–2147, <https://doi.org/10.5194/os-21-2125-2025>, 2025.
- 600 Kärnä, T., Ljungemyr, P., Falahat, S., Ringgaard, I., Axell, L., Korabel, V., Murawski, J., Maljutenko, I., Lindenthal, A., Jandt-Scheelke, S., and Verjovkina, S.: Nemo-Nordic 2.0: Operational marine forecast model for the Baltic Sea, *Geosci. Mod. Dev.*, 14, 5731–5749, <https://doi.org/10.5194/gmd-14-5731-2021>, 2021.
- LeBlond, P.H., and Mysak, L.A.: *Waves in the Ocean*, Elsevier Oceanography Series, Vol. 20, ISBN 9780080879772, 1981.
- 605 Lighthill, M.J., and Whitham, G.B.: On kinematic waves I. Flood movement in long rivers, *Proc. Royal Soc. London, Series A*, 229, 281–316, <https://doi.org/10.1098/rspa.1955.0088>, 1955.
- Luettich Jr, R.A., Carr, S.D., Reynolds-Fleming, J.V., Fulcher, C.W., and McNinch, J.E.: Semi-diurnal seiching in a shallow, micro-tidal lagoonal estuary, *Cont. Shelf Res.*, 22, 1669–1681, [https://doi.org/10.1016/S0278-4343\(02\)00031-6](https://doi.org/10.1016/S0278-4343(02)00031-6), 2002.
- Maas, L.R.: On the nonlinear Helmholtz response of almost-enclosed tidal basins with sloping bottoms, *J. Fluid Mech.*, 349, <https://doi.org/10.1017/S0022112097006824>, 1997.
- 610 Medvedev, I.P., and Kulikov, E.A.: Spectrum of Mesoscale Sea Level Oscillations in the Northern Black Sea: Tides, Seiches, and Inertial Oscillations, *Oceanology*, 56, 6–13, <https://doi.org/10.1134/S0001437016010094>, 2016.
- Medvedev, I.P.: Numerical Modeling of Meteorological Sea Level Oscillations in the Black Sea, *Oceanology*, 62, 471–481, <https://doi.org/10.1134/S0001437022040087>, 2022.
- 615 Medvedev, I.P., Rabinovich, A.B., and Šepić, J.: Destructive coastal sea level oscillations generated by Typhoon Maysak in the Sea of Japan in September 2020, *Sci. Rep.*, 12, 8463, <https://doi.org/10.1038/s41598-022-12189-2>, 2022.
- Méhauté, B. L., Wilson, B. W., Miles, J., and Munk, W.: Closure to “Harbor Paradox”, *J. Waterways Harbors Div.*, 88, 173–195, <https://doi.org/10.1061/JWHEAU.0000275>, 1962.
- Miles, J., and Munk, W.: Harbor paradox, *J. Waterways Harbors Div.*, 87, 111–132, <https://doi.org/10.1061/JWHEAU.0000223>, 1961.
- 620



- Miles, J.W., and Lee, Y.K.: Helmholtz resonance of harbours, *J. Fluid Mech.*, 67, 445–464, <https://doi.org/10.1017/S0022112075000407>, 1975.
- Miles, J.W.: Harbor seiching. *Ann. Rev. Fluid Mech.*, 6, 17–33, <https://doi.org/10.1146/annurev.fl.06.010174.000313>, 1974.
- Miller, A., and Luscher, A.: NOAA’s national water level observation network (NWLON), *J. Oper. Oceanogr.*, 12, S57–S66,
625 <https://doi.org/10.1080/1755876X.2018.1523301>, 2019.
- Mohr, S., Kunz, M., Richter, A., and Ruck, B.: Statistical characteristics of convective wind gusts in Germany, *Nat. Haz. Earth Syst. Sci.*, 17, 957–969, <https://doi.org/10.5194/nhess-17-957-2017>, 2017.
- Monserrat, S., Rabinovich, A.B., and Casas, B.: On the reconstruction of the transfer function for atmospherically generated seiches, *Geophys. Res. Lett.*, 25, 2197–2200, <https://doi.org/10.1029/98GL01506>, 1998.
- 630 Nakano, M., and Fujimoto, N.: Seiches in bays forming a coupled system, *J. Oceanogr. Soc. Japan*, 43, 124–134, <https://doi.org/10.1007/BF02111888>, 1987.
- Nesteckytė, L., Kelpšaitė-Rimkienė, L., and Rabinovich, A.B.: Hazardous meteotsunami-like sea-level oscillations in the Port of Klaipėda, the Baltic Sea, *Nat. Haz.*, 120, 2909–2928, <https://doi.org/10.1007/s11069-023-06311-4>, 2024.
- Panaiteșcu, F.V., Panaiteșcu, M., Panait, C., Scupi, A.A., Stan, L., Făitar, C., Sucișu, G., Silișcu, M., Ștefanescu, S., Capbun,
635 N., and Zlatev, N.: Metocean specifications for wind data base on the Black Sea, *J. Mar. Techn. Envir.*, 2, 58–64, <https://doi.org/10.53464/JMTE.02.2023.10>, 2023.
- Park, J., MacMahan, J., Sweet, W.V., and Kotun, K.: Continuous seiche in bays and harbors, *Ocean Sci.*, 12, 355–368, <https://doi.org/10.5194/os-12-355-2016>, 2016.
- Rabinovich, A.B.: Seiches and harbor oscillations. *Handbook of Coastal and Ocean Engineering* (edited by Y.C. Kim),
640 Singapore, World Scientific, 193–236, ISBN 9789814470605, 2009.
- Ramos-Alcántara, J., Agulles, M., Gomis, D., and Jordà, G.: Quantifying the contributors to extreme sea level events in a Mediterranean microtidal region at high spatio-temporal resolution, *Clim. Dyn.*, 63, <https://doi.org/10.1007/s00382-025-07653-4>, 2025.
- Ruić, K., Šepić, J., Mlinar, M., and Međugorac, I.: Contribution of high-frequency ($T < 2$ h) sea level oscillations to the
645 Adriatic sea level maxima, *Nat. Haz.*, 116, 3747–3777, <https://doi.org/10.1007/s11069-023-05834-0>, 2023.
- Sammartino, S., Garrido, J.S., Delgado, J., Naranjo, C., Aldeanueva, F.C., and Lafuente, J.G.: Experimental and numerical characterization of harbor oscillations in the port of Málaga, Spain, *Ocean Eng.*, 88, 110–119, <https://doi.org/10.1016/j.oceaneng.2014.06.011>, 2014.
- Seo, J.Y., Choi, B.J., Choi, S.M., Ryu, J., and Ha, H.K.: Contribution of coastal seiches to sediment transport in a microtidal semi-enclosed bay, *Front. Mar. Sci.*, 11, <https://doi.org/10.3389/fmars.2024.1392435>, 2024.
- 650 Šepić, J., Vilibić, I., Rabinovich, A.B., and Monserrat, S.: Widespread tsunami-like waves of 23–27 June in the Mediterranean and Black Seas generated by high-altitude atmospheric forcing, *Sci. Rep.*, 5, <https://doi.org/10.1038/srep11682>, 2015.



- Stanev, E.V., and Ricker, M.: The Fate of Marine Litter in Semi-Enclosed Seas: A Case Study of the Black Sea, *Front. Mar. Sci.*, 6, <https://doi.org/10.3389/fmars.2019.00660>, 2019.
- Stanev, E.V.: Understanding Black Sea dynamics: overview of recent numerical modelling, *Oceanography*, 18, 56–75, <https://www.jstor.org/stable/43925675>, 2005.
- Steinheuer, J., Beyrich, F., and Löhnert, U.: Exploiting the full potential of Doppler lidars: High-resolution wind-gust profiling in significant weather, *Quart. J. Royal Meteor. Soc.*, 151, e4961, <https://doi.org/10.1002/qj.4961>, 2025.
- 660 Sun, Q., and Niu, X.: Harbor resonance triggered by atmospherically driven edge waves, *Ocean Eng.*, 224, 108735, <https://doi.org/10.1016/j.oceaneng.2021.108735>, 2021.
- Teng, M.H., and Wu, T.Y.: Nonlinear water waves in channels of arbitrary shape, *J. Fluid Mech.*, 242, 211–233, <https://doi.org/10.1017/S0022112092002349>, 1992.
- Trukhchev, D., Bachvarova, E., Krastev, A., and Georgiev, S.: Features of the Hydrological Structure of Varna Lakes and
665 the Atmospheric Impact on the Water Area in the Period 2022–2023, *Proc. Bulg. Acad. Sci.*, 78, 873–883, <https://doi.org/10.7546/CRABS.2025.06.10>, 2025.
- Valiani, A., and Caleffi, V.: A one-dimensional augmented Shallow Water Equations system for channels of arbitrary cross-section, *Adv. Water Res.*, 189, <https://doi.org/10.1016/j.advwatres.2024.104735>, 2024.
- Vilibić, I., Denamiel, C., Zemunik, P., and Monserrat, S.: The Mediterranean and Black Sea meteotsunamis: an overview,
670 *Nat. Haz.*, 106, 1223–1267, <https://doi.org/10.1007/s11069-020-04306-z>, 2021.
- Vilibić, I., Zemunik Selak, P., and Šepić, J.: Meteorological tsunamis: from local hazard to global relevance, *Rev. Geophys.*, 63, e2024RG000867, <https://doi.org/10.1029/2024RG000867>, 2025.
- Williams, D.A., Horsburgh, K.J., Schultz, D.M., and Hughes, C.W.: Proudman resonance with tides, bathymetry and variable atmospheric forcings, *Nat. Haz.*, 106, 1169–1194, <https://doi.org/10.1007/s11069-020-03896-y>, 2021.
- 675 Yakushev, E., Berezina, A., Yakubov, S., Novikov, M., Ghaffari, P., Dzhurova, B., Hristova, O., Vogt, R., and Ranneklev, S.: Model-based analysis of seasonal hypoxia: The Varna Lake–Bay case study, *Ecol. Mod.*, 515, <https://doi.org/10.1016/j.ecolmodel.2026.111535>, 2026.
- Zheng, Z., Dong, G., and Ma, X.: Special modes with narrow amplification diagrams in harbor oscillations: definition and parametric study, *Ocean Dyn.*, 74, 511–523, <https://doi.org/10.1007/s10236-024-01616-9>, 2024.